

Physical Processes within the Nocturnal Stratus-topped Boundary Layer

CHIN-HOH MOENG AND SHAOHUA SHEN

*National Center for Atmospheric Research, * Boulder, Colorado*

DAVID A. RANDALL

Department of Atmospheric Science, Colorado State University, Fort Collins, Colorado

(Manuscript received 20 August 1991, in final form 8 January 1992)

ABSTRACT

Within the stratus-topped boundary layer many physical processes are involved: longwave radiation cooling, entrainment, latent heating, surface heating, solar heating, drizzling, etc. How all processes combine to maintain the turbulence within the stratus-topped boundary layer remains an unsolved problem. The large-eddy simulation technique is used to examine the first four physical processes mentioned. First, the contribution of each physical process to the thermodynamic differences between the updraft and downdraft branches of turbulent circulations is examined through a conditional sampling. Second, these mean thermodynamic differences are shown to express well the vertical distributions of heat and moisture fluxes within stratus-topped boundary layers.

These provide a method to validate the process-partitioning technique. (This technique assumes that the net flux profile can be partitioned into different component-flux profiles according to physical processes and that each partitioned component flux is linear in height.) In this paper, the heat and moisture fluxes are process partitioned, and each component flux is found to contribute to the net flux in a way that is consistent with its corresponding process contribution to the mean thermodynamic differences between updrafts and downdrafts. Also, the net flux obtained by summing all component fluxes agrees well with that obtained directly from the large-eddy simulations.

1. Introduction

The nocturnal, stratus-topped boundary layer has many important physical processes: longwave radiation, entrainment, surface heating, latent heating, drizzling, etc.—all working interactively and simultaneously in maintaining the turbulent circulations that transport momentum, heat, and moisture. How these processes combine to determine the turbulent transports is poorly understood, however, mainly for the following reasons. 1) Most of these processes occur (and interact) near the cloud top where the turbulent boundary layer and nonturbulent free atmosphere meet. 2) The strengths and the roles of these processes and their interactions vary in location along the cloud top (Nicholls 1989; Moeng and Schumann 1991). For example, more dry inversion air is entrained (i.e., engulfed) into downdrafts of major circulations, resulting

in more evaporative cooling there than in updrafts. This kind of information is lost when examining typical statistics, that is, quantities that are defined in terms of area averages.

Furthermore, careful and detailed observational studies of marine stratus are rare. One reason is that typical marine stratus is not normally found near shore, since continental effects can alter the boundary-layer structure and disrupt cloud persistence. As a result, most observational studies have relied heavily on long-range aircraft, which cannot provide much information on time evolution or the three-dimensional flow patterns. This, and the fact that observational data are affected by large-scale horizontal and diurnal variability and by decoupling of cloud layers, makes it difficult to study (or isolate) the physical processes, their interactions, and their roles.

In this study, we use the large-eddy simulation (LES) approach (Moeng 1984, 1986) for studying turbulent flows, which was first pursued by Deardorff in the early 1970s and has resulted in major advances in our understanding of the clear convective boundary layer (e.g., Deardorff 1974a,b; Moeng and Wyngaard 1984, 1986, 1989). The guidelines for its application to planetary boundary-layer (PBL) research were reviewed by Wyngaard (1984). Deardorff (1980a) and Moeng

* The National Center for Atmospheric Research is sponsored by the National Science Foundation.

Corresponding author address: Dr. Chin-Hoh Moeng, National Center for Atmospheric Research, P.O. Box 3000, Boulder, CO 80307-3000.

(1986, 1987) applied the LES approach to stratus-topped boundary layers. These simulations not only provide three-dimensional, time-dependent, stochastic fields of velocity, temperature, and moisture for detailed analysis, but also can be "controlled" so we can systematically examine each basic process involved.

In section 2, we describe the large-eddy simulated cases. In section 3, we review the convective mass-flux approach to boundary-layer modeling and examine the relationship between the turbulent fluxes and the thermodynamic differences between updraft and downdraft branches of the turbulent circulations. We then study the roles of several important physical processes in determining these updraft and downdraft properties (section 4) and in determining the vertical distributions of the total thermodynamic energy and moisture fluxes (section 5). We summarize and conclude this study in section 6.

2. The large-eddy simulations

Three large-eddy simulations of idealized nocturnal stratus-topped boundary layers have been carried out to study the relevant physical processes. These simulations used $80 \times 80 \times 80$ grids covering a numerical domain of $5 \text{ km} \times 5 \text{ km} \times 1 \text{ km}$. Therefore, they resolve turbulent eddies of sizes down to $125 \text{ m} \times 125 \text{ m} \times 25 \text{ m}$, twice the grid spacing. Moeng and Schumann (1991) have analyzed these LES data, but they studied just the composite coherent structures. This paper further analyzes these simulations to determine the relevant physical processes for generating and maintaining the turbulent transports. We discuss mainly 1) cloud-top longwave radiation, 2) entrainment, 3) surface heating, and 4) latent heating, which we believe are the most important mechanisms for maintaining or dissipating the *nocturnal* marine stratus. (Drizzling may also be important in dissipating the cloud, but will not be considered here.)

The three simulations of idealized stratus-topped PBLs are summarized in Table 1. The ENT/RAD simulation includes mainly the entrainment and longwave radiation processes. In this case, the surface heat flux is minimized. (Since we prescribed the sea surface temperature in the simulations, the surface heat flux cannot be exactly zero.) Latent heating was also excluded by using the "dust cloud" concept introduced

by Lilly (1968). In a dust cloud, "liquid water" can be "condensed" from or "evaporated" to water vapor, but *no* latent heating/cooling occurs. The ENT/RAD/SFC simulation includes entrainment, longwave radiation, and surface heating; latent heating is again excluded by considering a "dust cloud." The ENT/RAD/SFC/EVP simulation includes all four processes, and thus represents a realistic nocturnal, stratus-topped boundary layer. This simulation has been used by Schumann and Moeng (1991a,b) to study plume fluxes and budgets and by Randall et al. (1992) to test a mass flux model.

We can then study the effects of evaporation by comparing the ENT/RAD/SFC and ENT/RAD/SFC/EVP cases and the effects of surface heating by comparing the ENT/RAD and ENT/RAD/SFC cases. It is more difficult to separate the radiative cooling and entrainment processes since they always coexist in even the most idealized, prototype stratus cases. Therefore, we include in this study an LES of the clear convective boundary layer (CBL) that is driven mainly by surface heating. Since only surface flux and entrainment processes are involved, it is labeled ENT/SFC (also summarized in Table 1). The ENT/SFC case has been studied by Moeng and Wyngaard (1988, 1989), Schumann and Moeng (1991a,b), Moeng and Schumann (1991), and Wyngaard and Moeng (1992).

The statistics given in Table 1 are the average boundary-layer top height, z_i ; the average cloud-base height, z_B ; the friction velocity, u_* ; the surface buoyancy flux, $\overline{wS_{v0}}$; the convective velocity scale

$$w_* \equiv w_{c*} \equiv \left[\frac{g}{T_0} B_* z_i \right]^{1/3}$$

for the stratus cases and

$$w_* \equiv \left(\frac{g}{c_p T_0} z_i \overline{wS_{v0}} \right)^{1/3}$$

for the clear boundary-layer case; the temperature scale, $T_* \equiv B_*/w_{c*}$ for the stratus cases and $T_* \equiv \overline{wS_{v0}}/(c_p w_*)$ for the clear case; and the moisture scaling, $Q_* \equiv M_*/w_{c*}$ for the stratus cases only. Here

$$B_* \equiv \frac{1}{c_p} \int_{z_B}^{z_i} \overline{wS_v} dz / (z_i - z_B)$$

TABLE 1. Scaling parameters.

Experiments	PBL type	z_i (m)	z_B (m)	u_* (m s ⁻¹)	$\rho(\overline{wS_v})_0$ (W m ⁻²)	w_* (m s ⁻¹)	T_* (K)	Q_* (g kg ⁻¹)
(a) ENT/RAD	Dust cloud	475	199	0.32	10	0.8	0.04	0.010
(b) ENT/RAD/SFC	Dust cloud	476	203	0.33	38	0.81	0.04	0.015
(c) ENT/RAD/SFC/EVP	Wet cloud	509	234	0.30	27	0.88	0.04	0.020
(d) ENT/SFC	Clear	1027	—	0.59	240	2.0	0.12	—

and

$$M_* \equiv \int_{z_B}^{z_i} w(q_v + q_l) dz / (z_i - z_B)$$

are the vertically averaged buoyancy and moisture fluxes within the cloud layer; g/T_0 is the buoyancy coefficient; c_p is the specific heat of air; s_v is the virtual dry static energy; h_l is the liquid water static energy, a conserved quantity under both moist- and dry-adiabatic

processes (Moeng 1986); q_v is the water vapor mixing ratio; q_l is the liquid water mixing ratio; and w is the vertical velocity. The s_v and h_l fields have the dimensions of temperature after being divided by c_p . In the ENT/SFC simulation, moisture was not included; there the predicted thermal variable is s_v , which is conserved under dry-adiabatic processes. (The statistics shown here for the ENT/RAD/SFC/EVP case are from a later time period than the dust cloud cases, so

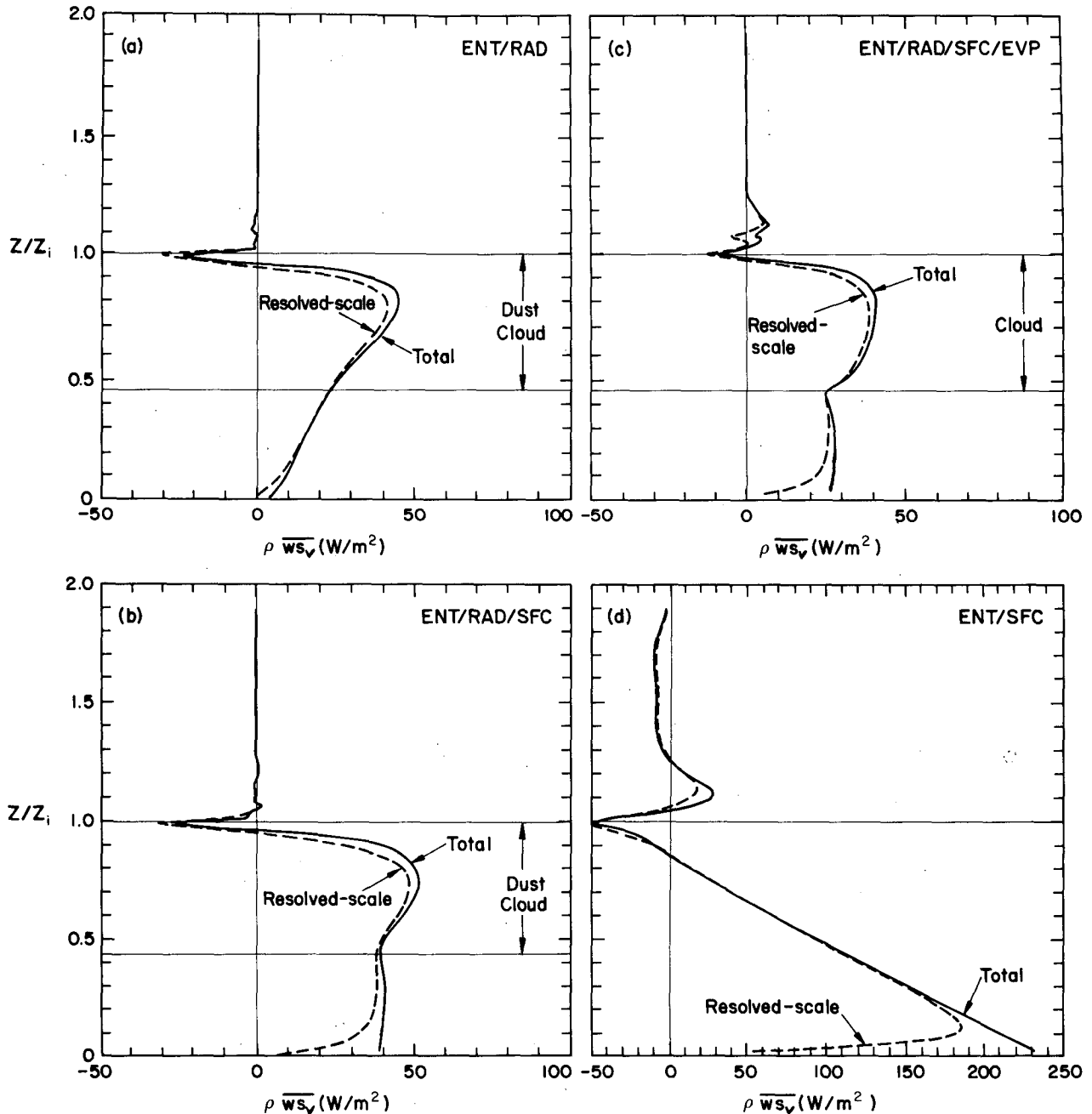


FIG. 1. Vertical distributions of the buoyancy fluxes from the four large-eddy simulations described in Table 1.

the cloud top is higher. The LES data of the earlier simulation period was not saved for the ENT/RAD/SFC/EVP case.)

The total (solid curves) and resolved (dashed) buoyancy fluxes for these four large-eddy simulations are given in Fig. 1. The upper left, the upper right is ENT/RAD/SFC/EVP (wet cloud case), and the lower right is ENT/SFC (clear PBL case). The dust or wet cloud layers are marked. The fluxes are shown in units of watts per square meter, and the height is normalized by z_i . The statistics are averages over horizontal surfaces and over a time period of about 2–3 large-eddy turnover times (six LES time records). (The local maximum above the boundary-layer top is likely due to numerical spuriousness, which is associated with difficulty of the advection scheme to handle the sharp temperature and moisture gradients; the longer the simulation period is, the larger the spurious maximum becomes.) Simulations ENT/RAD/SFC and ENT/RAD/SFC/EVP have their surface buoyancy fluxes (generated by surface heating) comparable to their near cloud-top buoyancy fluxes (generated by cloud-top radiative cooling). Note that the ENT/SFC case has a very strong surface buoyancy flux: 240 W m^{-2} .

The ENT/RAD/SFC/EVP (wet cloud) case has a smaller surface buoyancy flux (and a smaller surface moisture flux as well) than the ENT/RAD/SFC (dust cloud) case because of the following reason. The sea surface temperatures are the same in both cases. Since the analyzed LES field of ENT/RAD/SFC/EVP (wet cloud case) is from a later time period than other two stratus cases, it has a warmer and wetter PBL than ENT/RAD/SFC (dust cloud case), thus smaller surface fluxes. Although the LES simulations have reached a quasi-steady state, the mean temperature and moisture within the mixed layer are still changing in time. Therefore, the differences between ENT/RAD/SFC and ENT/RAD/SFC/EVP are not totally due to the latent heating effect. We will note the differences that resulted from this different time-period averaging wherever it applies.

3. The convective mass fluxes

Convective mass flux modeling, first applied by Arakawa (1969) and Betts (1976) in cumulus parameterization, is based on the idealization that convective circulations consist of two branches, updrafts and downdrafts, and that the turbulent fluxes associated with these circulations can be expressed by

$$\overline{wf} = M_c(f_u - f_d), \quad (1)$$

where $M_c = a(1-a)(w_u - w_d)$ is the convective mass flux, a is the area covered by updrafts, w_u and w_d are the mean vertical velocities of the updraft and downdraft branches, respectively, and f_u and f_d are the mean values of any scalars within the updraft and downdraft

(e.g., Randall 1987). This approach was recently applied to PBL parameterization by Chatfield and Brost (1987), Randall (1987), Wang and Albrecht (1990), and Randall et al. (1992). One of the closures in this type of modeling is determining M_c .

In developing techniques for measuring the turbulent fluxes, Businger and Oncley (1990) proposed a “relaxed eddy accumulation” method, in which the vertical turbulent flux of a scalar species f in the PBL is taken to be

$$\overline{wf} = b\sigma_w(f_u - f_d), \quad (2)$$

where b is a coefficient of proportionality and σ_w is the root-mean-square of the vertical velocity field. From data collected in the surface layer, Businger and Oncley found that b is about 0.6, independent of stability.

Wyngaard and Moeng (1992), using the joint probability density distribution of w and a scalar f generated from LES data, computed the Businger–Oncley parameter b in (2). They found $b \sim 0.6$ for a bottom-up scalar (i.e., a scalar with zero entrainment flux) and ~ 0.47 for a top-down scalar (i.e., a scalar with zero surface flux) throughout the whole CBL. They also showed analytically that for jointly Gaussian turbulence, $b = \sqrt{2\pi}/4 \sim 0.627$.

Moeng and Schumann (1991) show that turbulence driven by cloud-top radiative cooling has a less skewed vertical velocity field than that driven by surface heating. Therefore, the joint probability density of w and any scalar is expected to be more jointly Gaussian (i.e., $b \sim 0.6$) for the stratus-topped PBL than for the CBL. We generate, from the LES results, the joint density of w and h_l and of w and q_T , where q_T is the total moisture mixing ratio. Both joint density distributions are indeed approximately joint Gaussian, and $b \sim 0.6$ throughout most of the PBL. Instead of showing the b distribution, we compare $\overline{wh_l}$ (or $\overline{w\overline{s}_v}$ for the clear case) obtained by two methods: (a) directly correlating the resolved-scale w and h_l (or s_v for the clear case) fields of the LES data and (b) using Eq. (2) with $b = 0.6$. The result is shown in Fig. 2; the agreement is remarkably good for all cases. (We examine the resolvable field only since the subgrid scales cannot be split into updrafts and downdrafts.)

Figure 3 compares $\overline{wq_T}$ obtained (a) directly from the LES data and (b) by using Eq. (2) with $b = 0.6$. Again, the parameterized moisture flux is remarkably good. No moisture data are available for the CBL case.

As shown by Randall et al. (1992) with the “top-hat” model, the root-mean-square vertical velocity is given by $\sigma_w = \sqrt{a(1-a)(w_u - w_d)^2}$. Combining this with $M_c = a(1-a)(w_u - w_d)$ gives $b = \sqrt{a(1-a)}$. With this formula, the largest possible value of b is 0.5. This implies that if we use the top-hat model and require consistency between (1) and (2), the difference $f_u - f_d$ between the updraft and downdraft thermodynamic variables will have to be exaggerated by the top-

hat model in order to produce the correct fluxes. Further discussion is given by Randall et al. (1992).

The turbulent transports of heat and moisture are thus well expressed by the different properties of the updraft and downdraft branches. To see how the four processes under study here contribute to these turbulent transports, it is necessary to examine how they determine the properties within the updraft and downdraft branches separately.

4. Mean properties within the updrafts and downdrafts

a. Analysis methods

The local cloud-top height, $z_T(x, y)$, varies in time and space. Using conventional horizontal averaging, the statistics near the cloud-top level include both above-cloud and in-cloud properties. It is difficult to retrieve just the in-cloud properties from such an av-

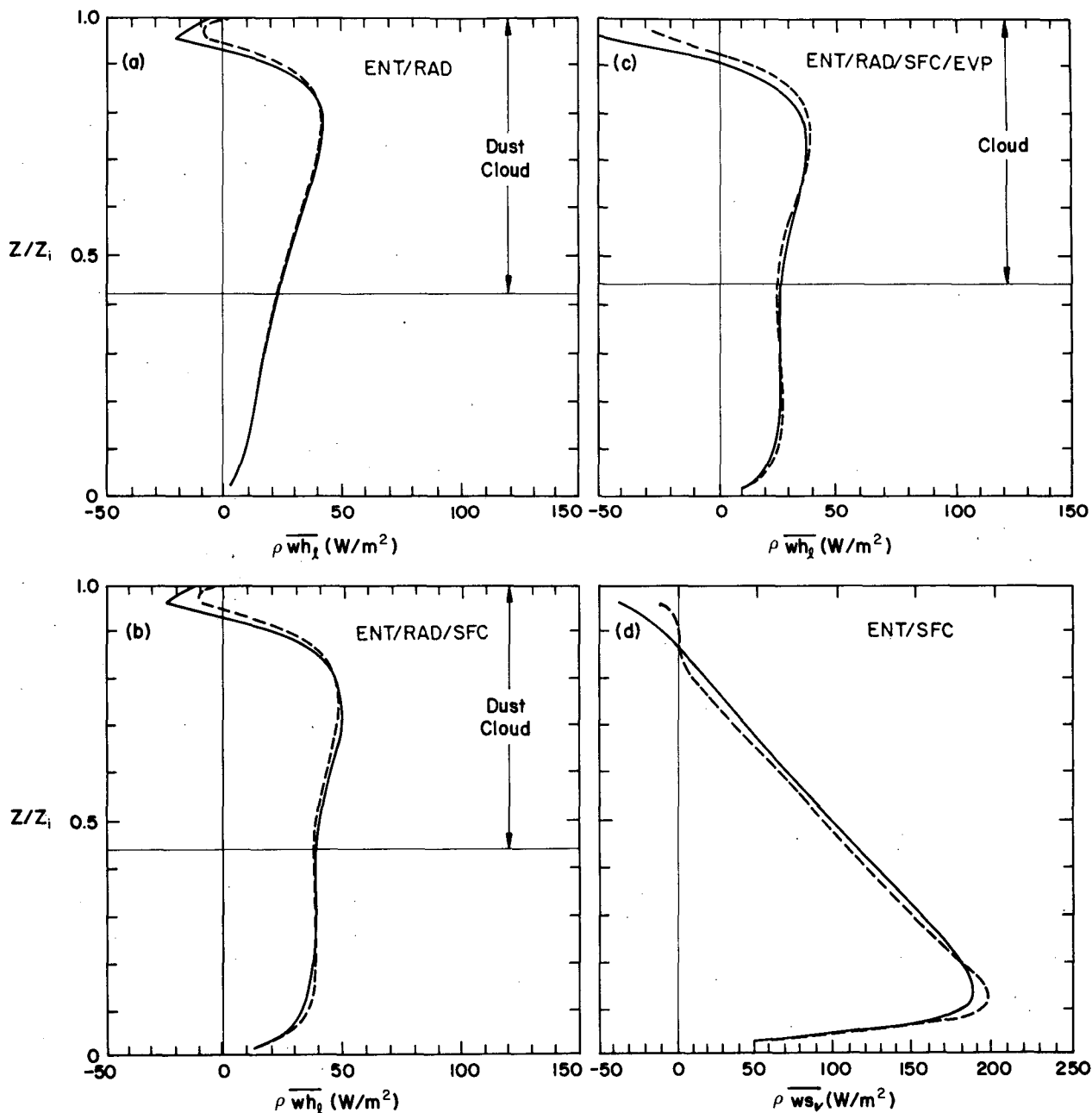


FIG. 2. Vertical distributions of \overline{wh}_i (or \overline{ws}_v for the clear case). The solid curves are obtained by correlating the resolved-scale w and h_i (or s_v) of the large-eddy simulated field, and the dashed curves are from (2) with $b = 0.6$.

eraging. We therefore perform a new averaging process. All variables at each LES grid column are scaled with the local cloud-top height. That is, we first interpolate the variables at each (x, y) grid column into a new vertical coordinate that puts all the local cloud-top heights at the same level in the new vertical grids and we then perform "horizontal" averaging over the new vertical coordinate, which consists of "hilly" surfaces parallel to the "hilly" cloud-top surface. This type of averaging was mentioned by Lilly and Schubert (1980) and used by Nieuwstadt and Businger (1984). The new "horizontally" averaged statistics will be slightly different, especially near the PBL top, from conventional statistics calculated by averaging over flat horizontal surfaces.

It is harder to perform this type of averaging in the clear convective case since there is no cloud top to serve as a reference. Instead, the temperature profiles at each grid column are used; the local PBL top, $z_T(x, y)$, is defined as the height where the temperature increases by at least 0.16 K across one grid interval ($\Delta z \sim 20$ m). The average of $z_T(x, y)$ defined this way equals approximately z_i (the height of the minimum buoyancy flux).

This averaging method is used only in this section to show the updraft-downdraft properties. Statistics represented by this new "horizontal" averaging will be presented in figures that have their height coordinate as $z/z_T(x, y)$. In other sections of this paper, statistics

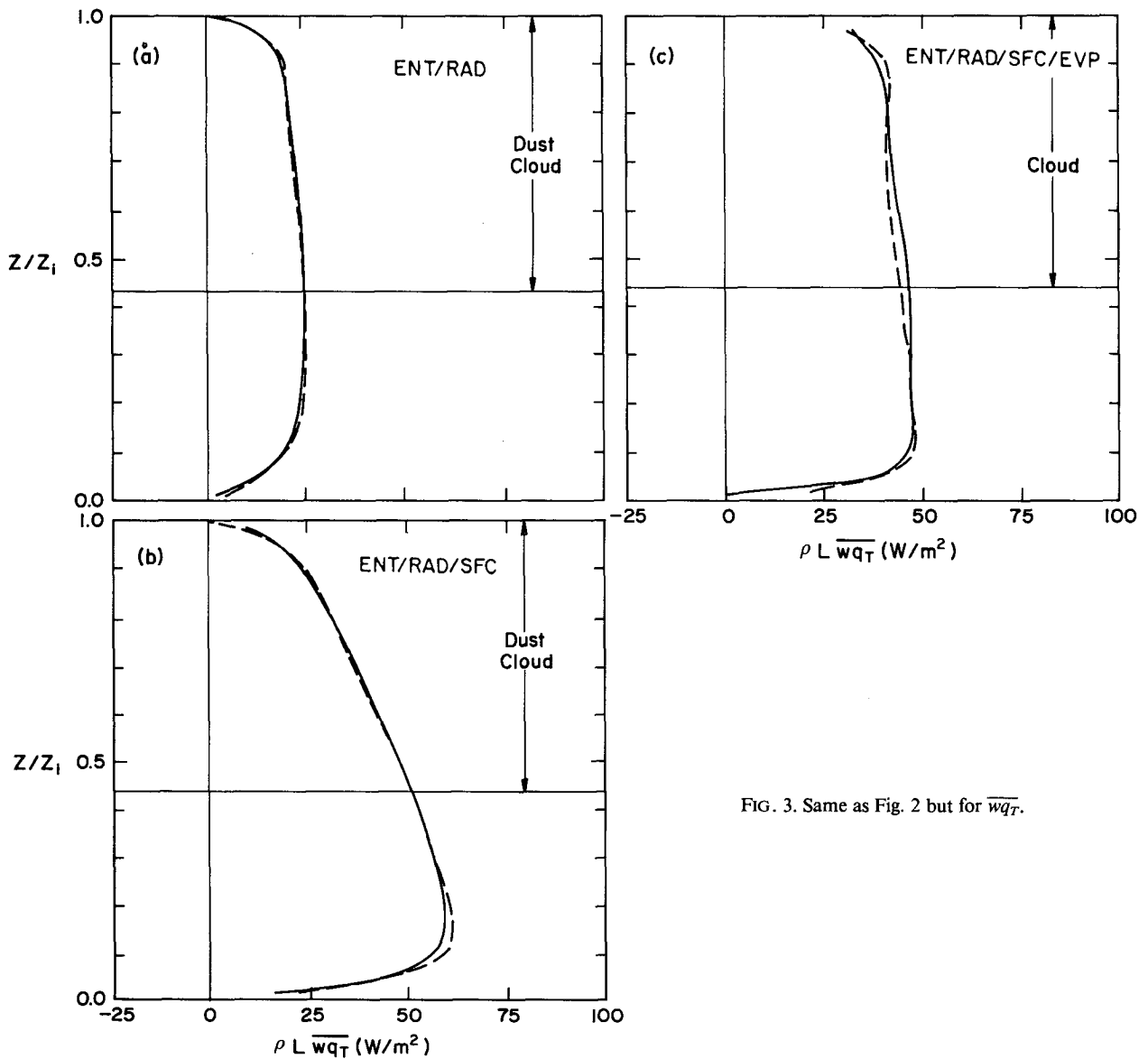


FIG. 3. Same as Fig. 2 but for $\overline{wq_T}$.

are represented by conventional horizontal averaging and the figures use the z/z_i height coordinate.

We also perform conditional sampling to separate the updraft and downdraft branches of the circulations. The vertical velocity fluctuations are used as an indicator: $w > 0$ for the updraft branch and $w < 0$ for the downdraft branch. This conditional sampling technique has been used by many others (e.g., Greenhut and Khalsa 1987; Young 1988; Schumann and Moeng 1991a).

Some research (S. J. S. Khalsa, personal communication) suggests that positive vertical velocity fluctuations near the PBL top do not necessarily coincide with the updrafts of major circulations. Therefore, using *local* vertical velocity as an indicator for splitting the updraft and downdraft branches of the dominant circulations may be inappropriate. Thus, a different type of conditional sampling was also performed that splits the updraft and downdraft branches according to the vertical velocity fluctuations in the middle of the PBL. Even though the results (not shown) differ quantitatively from those using the local vertical velocity field as the indicator, the results presented below are applicable to this type of sampling as well. In the

tuations near the PBL top do not necessarily coincide with the updrafts of major circulations. Therefore, using *local* vertical velocity as an indicator for splitting the updraft and downdraft branches of the dominant circulations may be inappropriate. Thus, a different type of conditional sampling was also performed that splits the updraft and downdraft branches according to the vertical velocity fluctuations in the middle of the PBL. Even though the results (not shown) differ quantitatively from those using the local vertical velocity field as the indicator, the results presented below are applicable to this type of sampling as well. In the

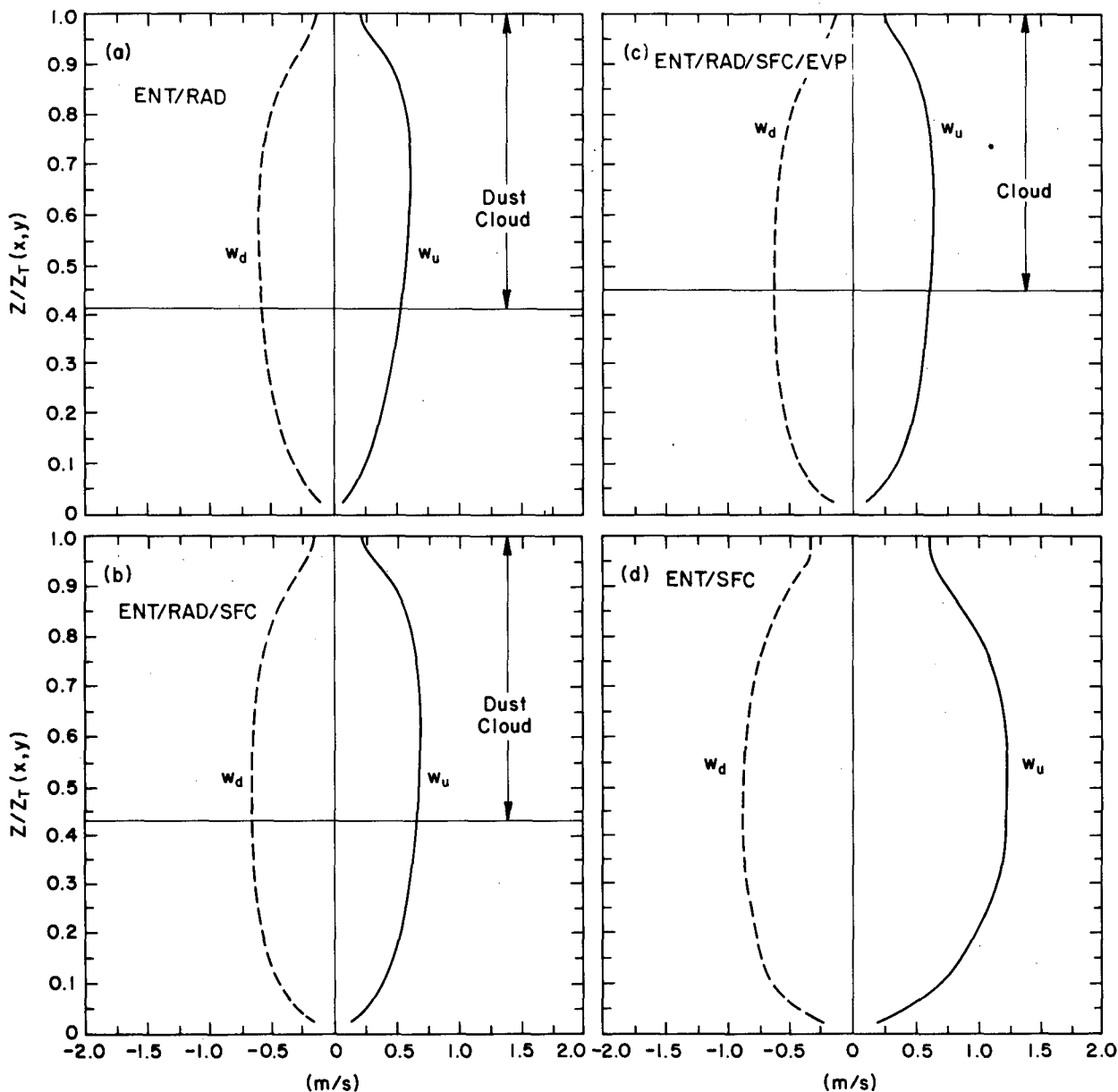


FIG. 4. Vertical distributions of the mean vertical velocities within updrafts (solid curves) and within downdrafts (dashed curves) deviating from the "horizontal" mean value.

following, our definition of the updraft branch is a collection of all the ascending elements, and that of the downdraft branch a collection of all the descending elements.

b. Results and discussion

The solid and dashed curves in Figs. 4, 5, 6, and 7 show the vertical distributions of the mean properties within the updraft branch and downdraft branch, respectively. The four panels are for the different LES

cases. These figures show, in order, the vertical velocity, virtual temperature, total moisture, and liquid water mixing ratio that are “horizontally” averaged (over the “hilly” surface) within updrafts and within downdrafts, respectively. The “horizontal” means that are subtracted out in these figures have similar profiles to the conventional horizontal-mean profiles; the latter for ENT/RAD/SFC/EVP (wet cloud) and ENT/SFC (clear PBL) cases can be found in Schumann and Moeng (1991a).

The vertical velocity differences between updrafts and downdrafts for all three stratus cloud cases are

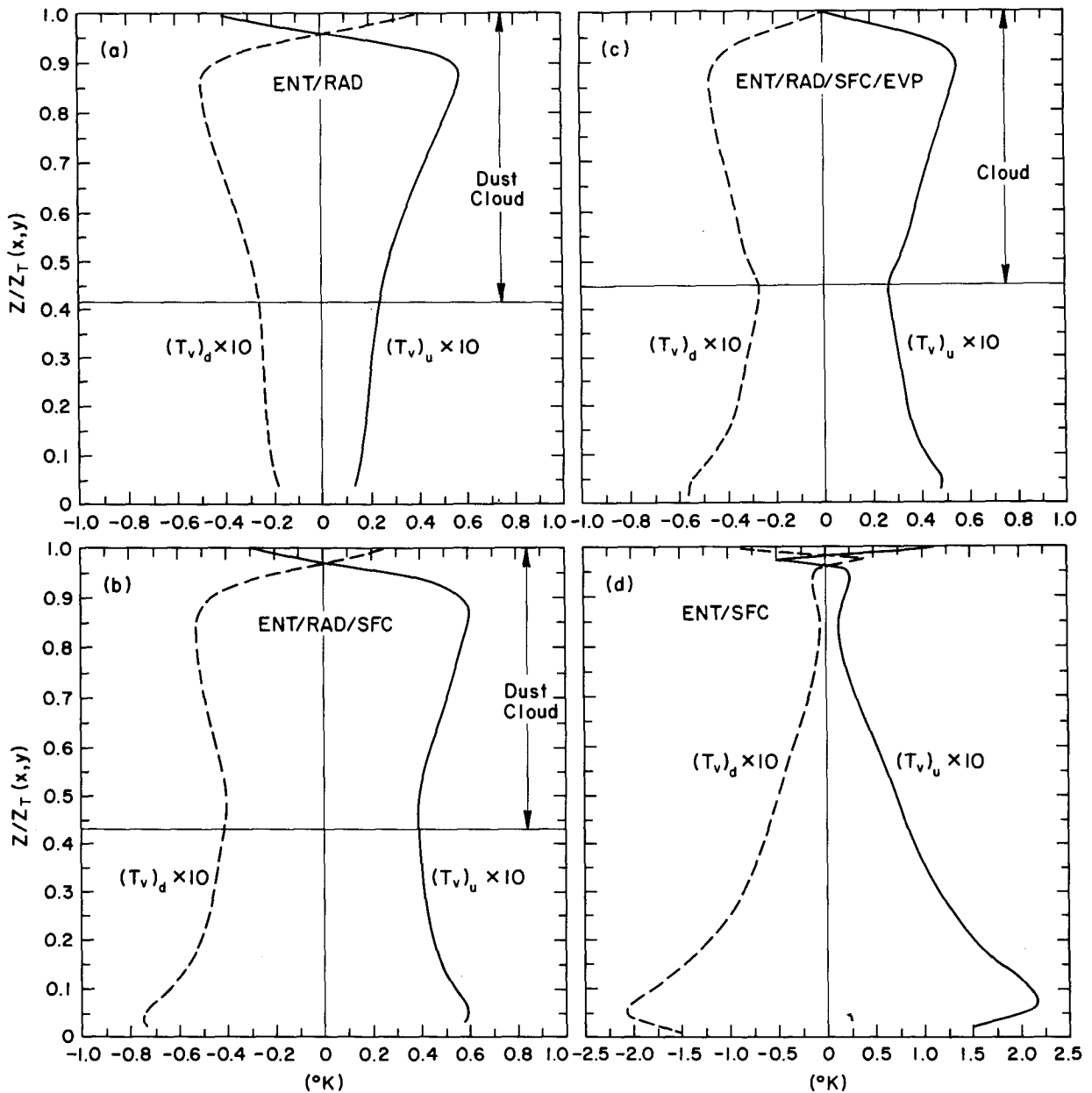


FIG. 5. Same as Fig. 4 but for the virtual temperature field.

within 30%; the addition of surface heating to cloud-top radiative cooling increases the circulations (measured as $w_u - w_d$) by about 30% in the lower PBL. The circulations in the ENT/SFC (clear PBL) case are particularly strong since the input surface buoyancy flux is particularly large (Fig. 1). Updrafts are about twice as strong as downdrafts in the ENT/SFC case; that is, the CBL has a positively skewed vertical velocity field, as discussed in Moeng and Schumann (1991).

Figure 5 shows the mean virtual temperature differences between the updrafts and downdrafts. Within the upper 5% of the dust-cloud-topped PBL (i.e., in the ENT/RAD and ENT/RAD/SFC cases where the evaporation/condensation effect is neglected), the up-

draft branch is colder than the downdraft branch. [Note that within this 5% layer, the air is totally cloudy since the height is scaled with $z_T(x, y)$.] In the upper part of the updraft, there is less entrained inversion air and also there is adiabatic lifting; both contribute in making the updrafts colder than the downdrafts in this uppermost layer. When evaporative cooling is included, however, as in the ENT/RAD/SFC/EVP (wet cloud) case, the downdrafts become colder than updrafts everywhere. Apparently, cloud-top evaporation cools downdrafts more than updrafts, because more dry air is engulfed into downdrafts. This latent heating contribution to the updraft-downdraft differences offsets the net effect from entrainment and adiabatic lifting,

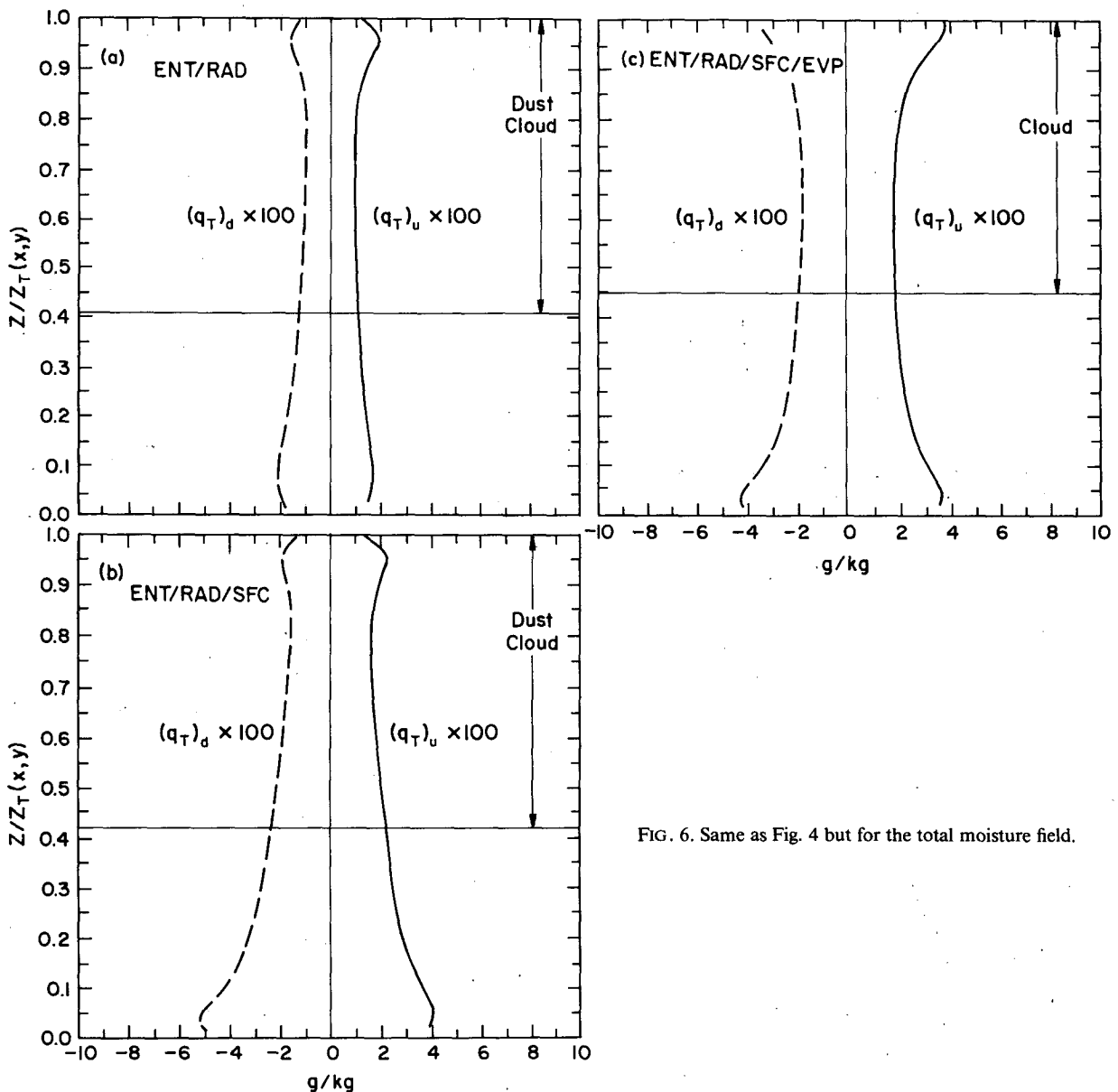


FIG. 6. Same as Fig. 4 but for the total moisture field.

resulting in colder downdrafts. Later, the liquid water field, given below, will be used to estimate this contribution.

Within the mixed layer, updrafts are warmer than downdrafts, so the turbulent circulations are buoyantly driven. The surface heating in the ENT/RAD/SFC (dust cloud) case results in much larger temperature variations in the lower half of the PBL than in the ENT/RAD (dust cloud) case; consequently, the heat flux is much larger there, as will be shown in section 5. The latent heating causes smaller temperature variations near the cloud base in ENT/RAD/SFC/EVP (wet cloud) than in the ENT/RAD/SFC (dust cloud) case. This seems to imply that condensation heats

downdrafts more than updrafts, which is puzzling. (The difference in the lower PBL between the ENT/RAD/SFC and ENT/RAD/SFC/EVP cases is mainly due to the fact that their statistics are taken from a different time period.)

The updraft-downdraft temperature differences are more height dependent in the ENT/SFC (clear PBL) case than in the stratus cases because of entrainment. Entrainment brings more warm air into downdrafts than updrafts and reduces the updraft-downdraft temperature differences from surface heating. This effect is greatest at the PBL top and decreases downward, while the surface heating effect has a maximum at the surface and decreases upward. For the stratus cases,

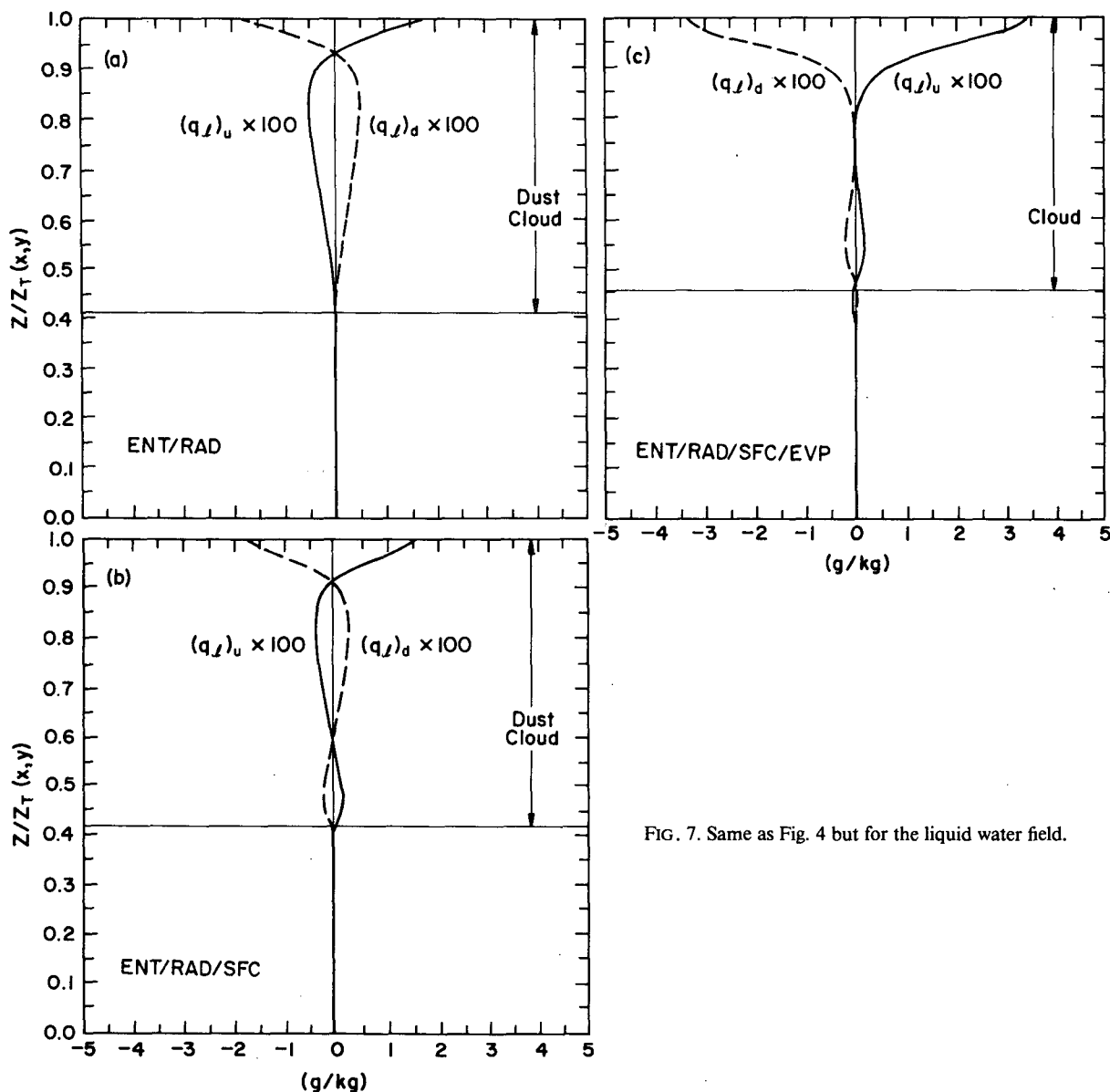


FIG. 7. Same as Fig. 4 but for the liquid water field.

the reduction of $(T_v)_u - (T_v)_d$ due to entrainment works concurrently with the enhancement of $(T_v)_u - (T_v)_d$ due to cloud-top radiative cooling, thus resulting in less height dependence of $(T_v)_u - (T_v)_d$.

Figure 6 shows the mean moisture differences between the updrafts and downdrafts. The updrafts are always wetter than the downdrafts throughout the whole PBL as a result of both surface and entrainment processes. (The radiation and evaporation processes do not contribute to the total mixing ratio.) Even though the surface buoyancy flux is negligibly small in the ENT/RAD (dust cloud) case, there is a significant surface moisture flux because the saturated mixing ratio at the ocean surface is much larger than the mixing ratio within the PBL. Therefore, the moisture differences between updrafts and downdrafts in the ENT/RAD (dust cloud) case are due to both entrainment-drying and surface-moistening processes. Including the surface-heating process in the ENT/RAD/SFC (dust cloud) case results in moisture differences almost twice as large as in the ENT/RAD (dust cloud) case. Latent heating seems to have little effect. (The difference in the lower PBL between the ENT/RAD/SFC and ENT/RAD/SFC/EVP cases is mainly due to the fact that their statistics are taken from a different time period.)

The liquid-water mixing ratio (Fig. 7) is larger within the upper 10% of the updrafts than downdrafts. This is due to a larger total mixing ratio in the updrafts. The differences in q_l can contribute to the evaporative cooling only in the ENT/RAD/SFC/EVP (wet cloud) case where the latent heating effect is included. We can estimate the temperature differences between the updrafts and downdrafts due to evaporative cooling as follows. Assume that the updraft-downdraft temperature differences due to evaporative cooling are $L[(q_l)_u - (q_l)_d]/c_p$, where $(q_l)_u - (q_l)_d \sim 7 \times 10^{-2} \text{ g kg}^{-1}$ at the cloud-top level (from Fig. 7c). Thus, the evaporation contribution alone gives $T_u - T_d \sim 0.17 \text{ K}$. This is more than enough to bring the downdrafts at the cloud top in the dust-cloud cases (which are only about 0.06 K warmer in ENT/RAD/SFC) to nearly the same temperature as updrafts in the real cloud case. Since the liquid water differences vary between the ENT/RAD/SFC/EVP (wet cloud) and ENT/RAD/SFC (dust cloud) cases, it is difficult to exactly figure out the evaporation effect. We also note that within the mixed layer, the liquid water differences between updrafts and downdrafts inexplicably change from case to case.

The solid and dashed curves in Fig. 8 show the mean longwave radiative fluxes within the updrafts and downdrafts, respectively. We compute $(F_{\text{rad}})_u$ and $(F_{\text{rad}})_d$ by vertically integrating the radiative cooling rate at each (x, y) column and averaging over updrafts and downdrafts, respectively. (The longwave radiative cooling rate at each grid point in the LES records has been saved.) Well within the cloudy layer, the radiative

fluxes are set to zero as a reference for the integration. We multiply the flux by c_p to obtain units of watts per square meter. The mean longwave radiative fluxes within the updrafts and downdrafts differ slightly; the flux jump (i.e., the slope) near the cloud top is slightly larger in the updraft branch than in the downdraft branch.

An interesting feature is that about 10% of the flux jump is *above* the cloudy layer [i.e., above $z_T(x, y)$], not too different from that observed by Slingo et al. (1982) and reported by Nieuwstadt and Businger (1984). As will be seen in section 5, F_{TOP} —the mean longwave radiative flux averaged along the “hilly” $z_T(x, y)$ surface—is about 10% smaller than the average F_{rad} at the z_i level. We define $\Delta F \equiv F_{\text{TOP}} - (F_{\text{rad}})_0$, which is the bulk-flux jump across the whole turbulent layer, where $(F_{\text{rad}})_0$ is the radiation flux at the surface. Since only the radiative cooling (i.e., the flux jump) that is *entirely within* the turbulent layer can drive the turbulent circulations *directly* (e.g., Kahn and Businger 1979), ΔF will be used in section 5 to partition the total thermodynamic energy flux profile.

The radiative cooling *above* the cloudy layer [i.e., above $z_T(x, y)$] may cool the inversion air and make the entrainment process easier. In that sense, the radiative cooling above $z_T(x, y)$ may be important in determining the entrainment rate and thus may *indirectly* affect the turbulent transports. In this paper, however, the problem of determining entrainment rate will not be addressed.

c. Summary

To conclude this section, the roles of each physical process in determining the mean properties within updrafts and downdrafts are summarized separately.

1) Moeng and Schumann (1991) show that downdrafts near the cloud top are initially forced as the horizontal flow converges. As downdrafts are forced downward into the mixed layer, more radiatively cooled air parcels are incorporated into them than into updrafts. This way, cloud-top radiative cooling contributes to colder downdrafts than updrafts, thus buoyantly driving the whole turbulent circulations. In this sense, only the cloud-top radiative flux jump that is within the cloudy layer can actually drive the turbulent circulations and contribute directly to the turbulent fluxes.

2) Entrainment brings warm and dry inversion air into the PBL, mostly into the downdrafts. Thus, entrainment tends to make the downdrafts warmer than the updrafts throughout the whole depth of the PBL. In the absence of surface heating, only when cloud-top radiative cooling dominates entrainment can the PBL be buoyantly driven. Entrainment also gives drier downdrafts than updrafts throughout the PBL.

3) Surface heating (and surface moistening) seems to be more efficient, in comparison with the cloud-top

radiative cooling process, in producing warmer (and wetter) updrafts than downdrafts. The updraft–downdraft temperature differences in the lower half of the ENT/RAD/SFC are shown to be more than twice as large as in the ENT/RAD case. The updraft–downdraft moisture differences also increase, largely due to surface effects.

4) Evaporative cooling is larger in downdrafts than updrafts within the upper 5% of the cloud-top layer since there is more entrained dry air within downdrafts. This cooling overcomes other processes, and, as a net result, downdrafts become colder than updrafts also in that layer, as shown in Fig. 5c. In our simulated cloud case, which is stable with respect to the cloud-top entrainment instability, the latent heating contribution

seems to be confined to this thin top layer; it seems to contribute very little to the overall turbulent circulations or to the overall heat and moisture variations. When the cloud-top entrainment instability condition is satisfied, this process may become more significant, and a strong evaporation–entrainment interaction may then contribute to a breakup of the stratus deck (Lilly 1968; Randall 1980a; Deardorff 1980b; Albrecht et al. 1985; MacVean and Mason 1990).

5. Contributions of processes to the vertical distributions of the turbulent fluxes

In section 3, the turbulent fluxes were shown to be well expressed by the differences between the ther-

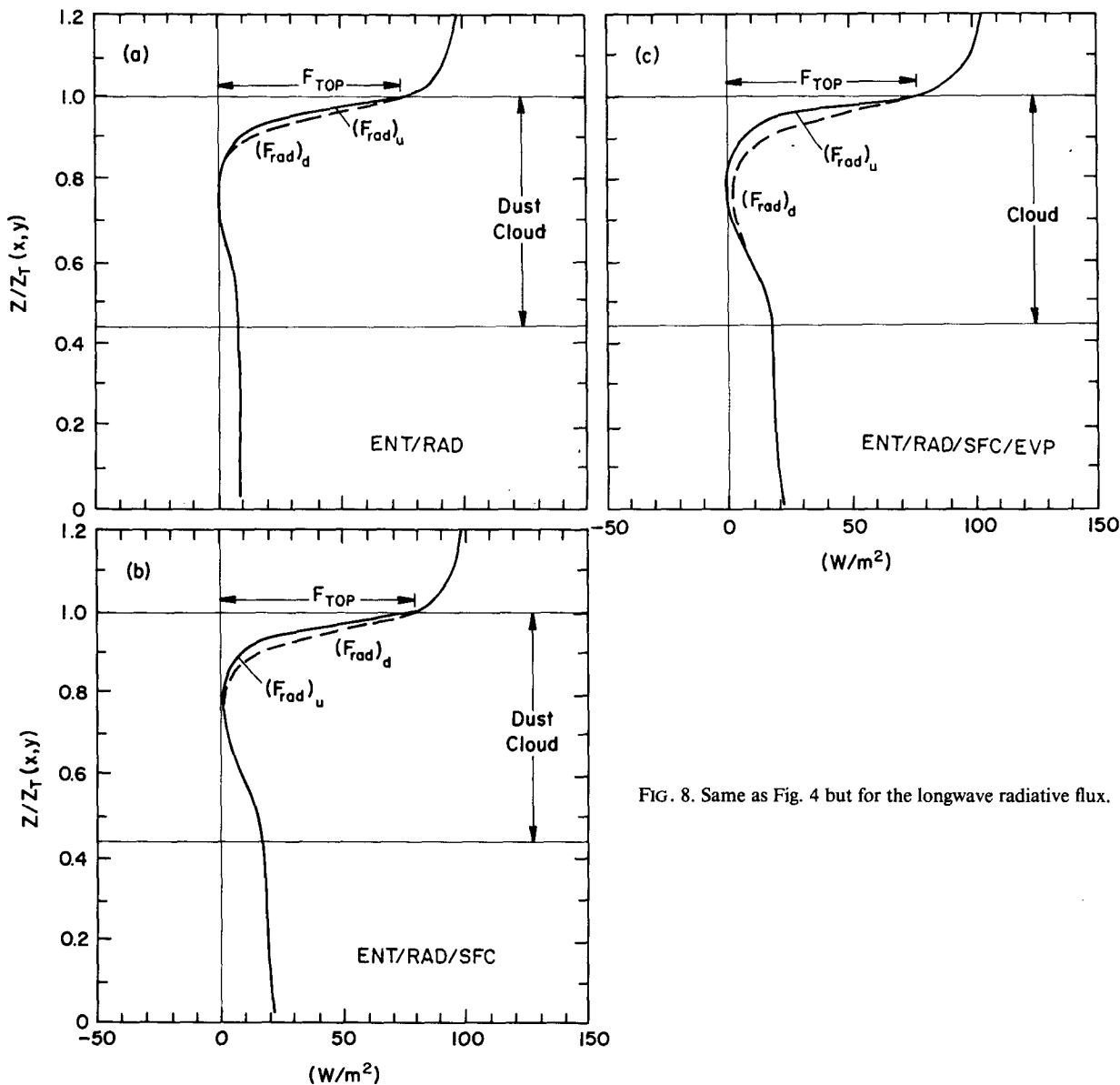


FIG. 8. Same as Fig. 4 but for the longwave radiative flux.

modynamic properties of the updrafts and downdrafts. We have also qualitatively examined the contributions of each physical process to such differences in section 4. Based on that, the linear "process partitioning" of the heat and moisture fluxes will be examined. Process partitioning, first proposed by Manins and Turner (1978) and labeled by Randall (1984), is a parameterization that separates the roles of various physical processes in determining the flux profiles. It was used by Stage and Businger (1981), Wilczak and Businger (1983), and Hanson (1987a) to partition the buoyancy flux within the convective PBL. It assumes that each partitioned flux is linear in height and that the linear sum of all partitioned fluxes represents the total flux.

Here, we will partition the total thermodynamic energy flux and the total moisture flux since they are linear in height for a homogeneous, quasi-steady-state boundary layer and are therefore easier to partition.

a. Partitioning the thermodynamic energy flux

Figure 9 shows the total thermodynamic energy flux, $H \equiv \rho w h_l + F_{rad}$ (solid curves), and the longwave radiative flux, F_{rad} (dashed curves), for all three stratus cases, where the air density ρ is 1 kg m^{-3} in our simulations. Here the statistics are the conventional averages over x - y horizontal planes and over 2 ~ 3 large-

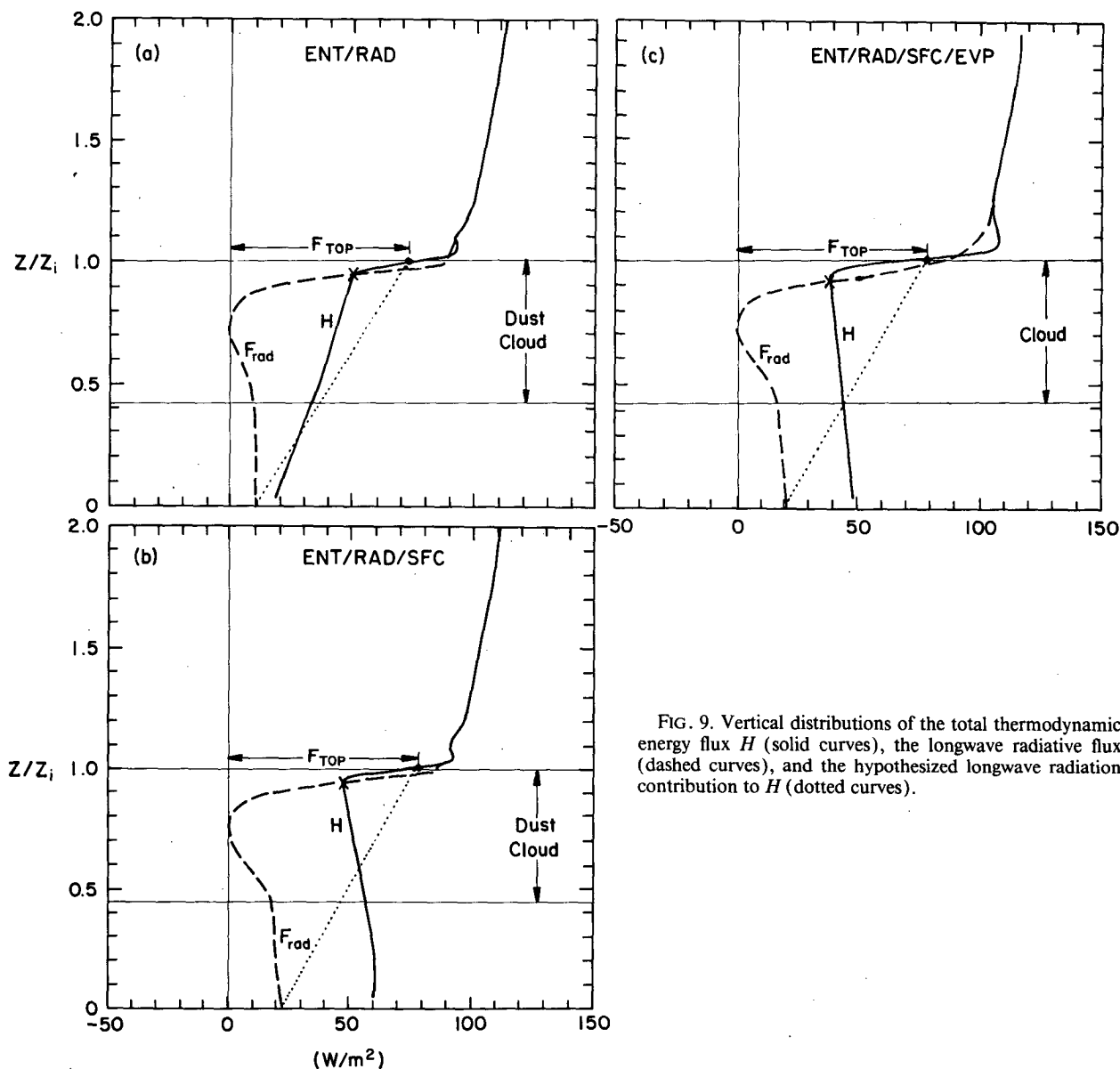


FIG. 9. Vertical distributions of the total thermodynamic energy flux H (solid curves), the longwave radiative flux (dashed curves), and the hypothesized longwave radiation contribution to H (dotted curves).

eddy turnover times. Thus, F_{rad} is the horizontally averaged radiative flux. The total thermodynamic energy flux should be linear in height within the mixed layer (i.e., below $\sim 0.95 z_i$ level marked by \times in Fig. 9) for a homogeneous, quasi-steady boundary layer because

$$\rho \frac{\partial}{\partial t} \left(\frac{\partial \bar{h}_l}{\partial z} \right) = - \frac{\partial^2 H}{\partial z^2} = 0. \quad (3)$$

As discussed in section 4, only the radiative flux jump that is within the solid cloud layer (i.e., the turbulent layer) is available for driving the turbulence directly. Some of the flux at z_i is actually above the solid

cloud layer and should be excluded. We hypothesize here that the dotted curves in Fig. 9, which are the linear curves that have F_{TOP} at z_i and $(F_{\text{rad}})_0$ at the surface, are the H -flux component response to an external forcing of only longwave radiation. Using F_{TOP} [the average radiative flux along the $z_T(x, y)$ surface] instead of $F_{\text{rad}}(z_i)$ excludes the above-cloud radiation effect on turbulent transports. For the ENT/RAD (dust cloud) case, where the surface heating is negligibly small for example, H is smaller than the dotted curve throughout the PBL because of entrainment. In other words, entrainment reduces H , and thus $\bar{w}h_l$, for a given longwave radiation forcing.

Figure 10 shows the vertical distributions of $\bar{w}h_l$ from

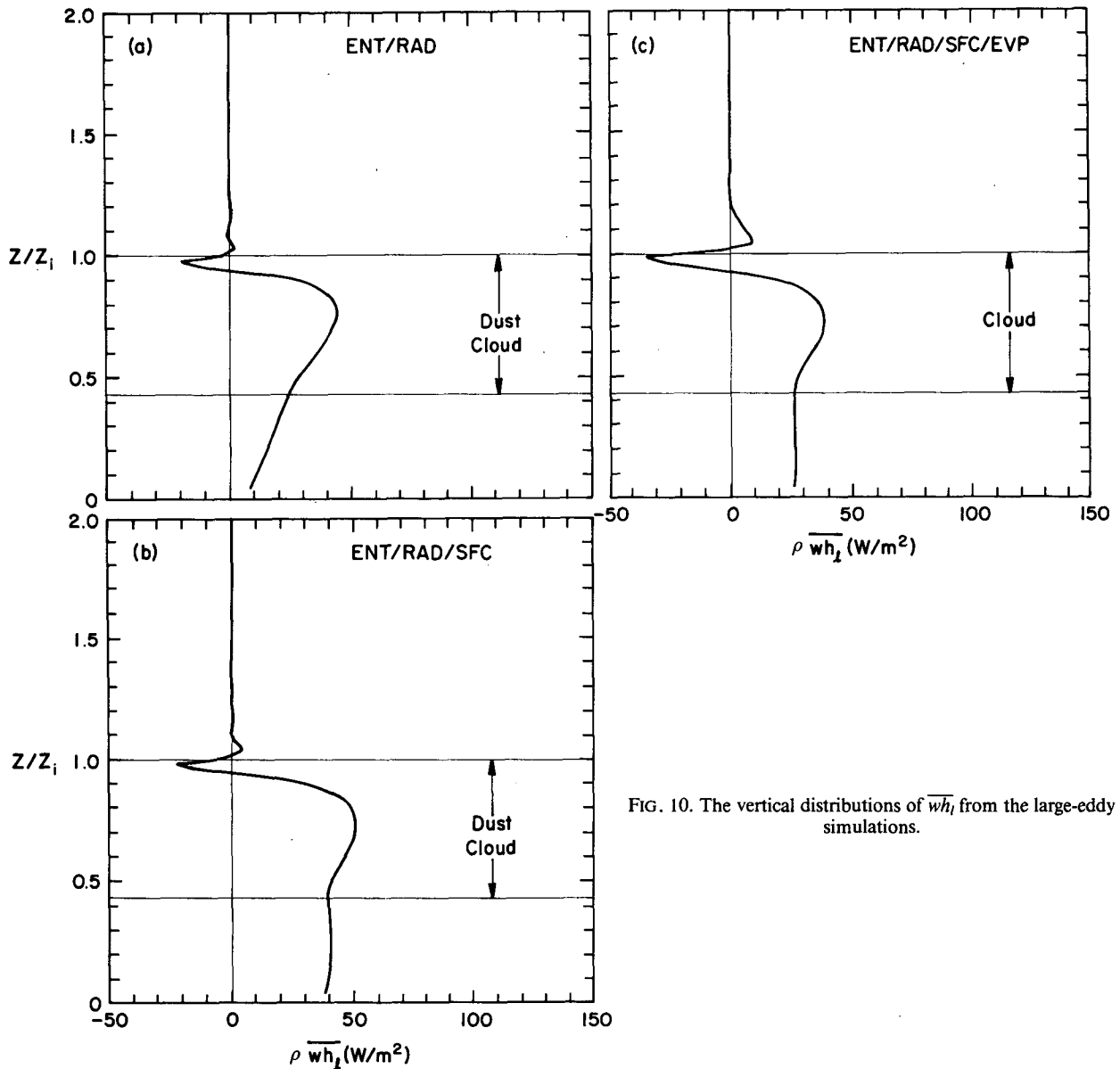


FIG. 10. The vertical distributions of $\bar{w}h_l$ from the large-eddy simulations.

the LES results. Note that they are not linear with height because F_{rad} is not linear.

From the above argument, we partition the profile of H in Fig. 11 according to the various physical processes involved. Assume that the contribution of each process is linear with height, as suggested by Stage and Businger (1981) and as implied from the analysis of section 4. For convenience, the x coordinates of Fig. 9 are shifted to those of Fig. 11 to eliminate the surface radiation flux (which should not affect the turbulent transports anyway). Note that $\Delta F = F_{\text{TOP}} - (F_{\text{rad}})_0$.

[ΔF is larger in ENT/RAD than in ENT/RAD/SFC and ENT/RAD/SFC/EVP because 1) the net long-wave radiative flux along the cloud top (i.e., F_{TOP}) is about the same for all three cases, and 2) the ENT/RAD case has a smaller sea surface temperature and thus a smaller $(F_{\text{rad}})_0$.]

The solid curves in Fig. 11 are the H profiles in Fig. 9 after the coordinate shift. The H -flux component response to the cloud-top radiative cooling process alone is represented by the RAD curves, which are ΔF at z_i and zero at the surface. The component response to

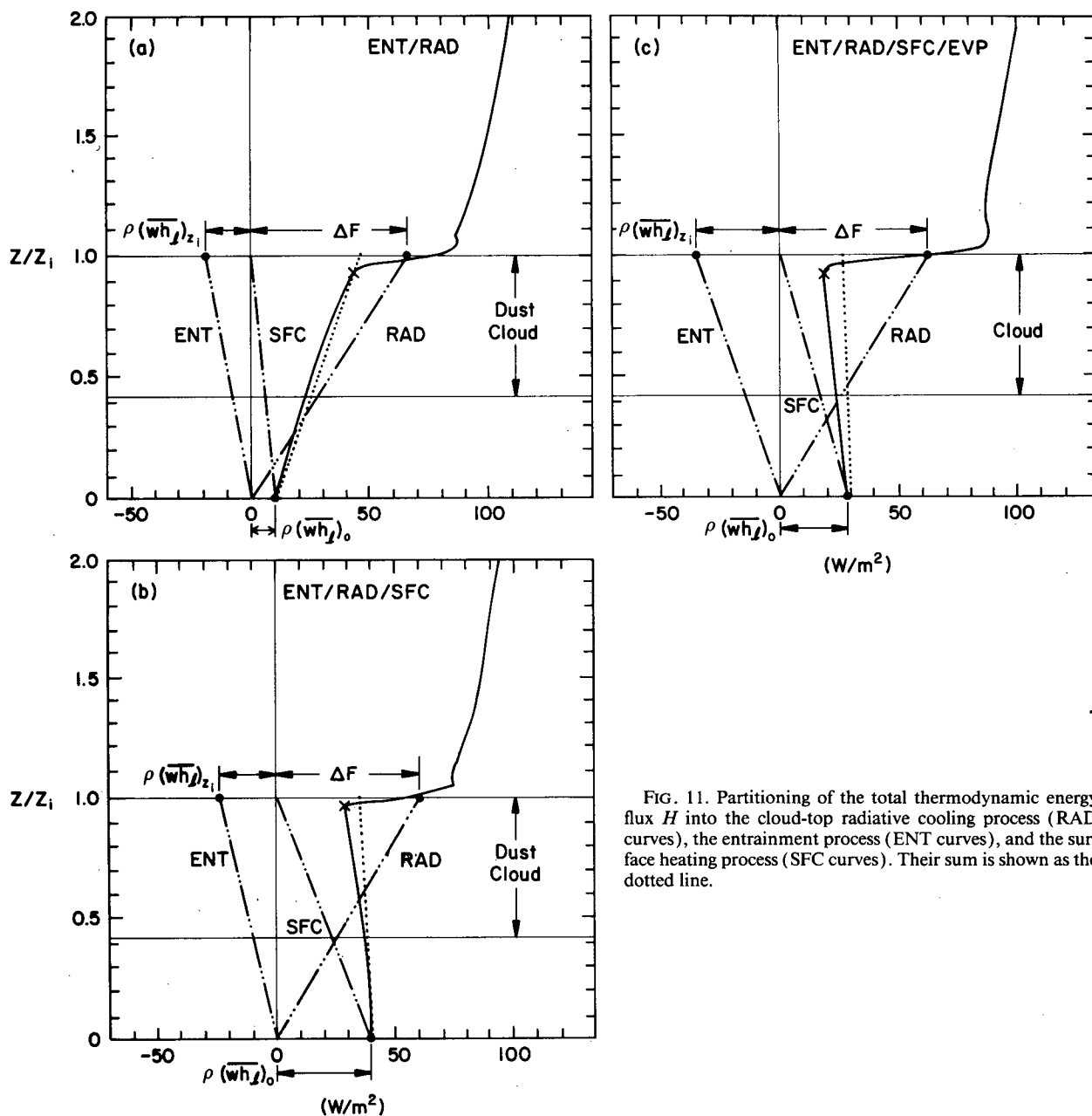


FIG. 11. Partitioning of the total thermodynamic energy flux H into the cloud-top radiative cooling process (RAD curves), the entrainment process (ENT curves), and the surface heating process (SFC curves). Their sum is shown as the dotted line.

the entrainment process alone is represented by the ENT curves, which are $(\overline{wh}_l)_{z_i}$ at z_i and zero at the surface. The component response to the surface-heating process alone is represented by the SFC curves, which are $(\overline{wh}_l)_0$ at the surface and zero at the top. (The latent heating should not affect the H profile since h_l is conserved under a moist-adiabatic process.) The sum (dotted lines) of these three curves gives approximately the H profile computed from the LES data (solid curves).

Our process partitioning is basically the same as that proposed by Stage and Businger (1981), Hanson (1987a), and Stull (1988, his Fig. 13.20) and discussed by Randall (1984). However, since we partition the H profile, not \overline{ws}_v or \overline{wh}_l , the vertical distribution of the radiative flux does not affect the partitioning. It is shown that F_{rad} is not linear with height, so that \overline{wh}_l (or the equivalent potential temperature flux) is not linear either. The details of the F_{rad} distribution will modify the \overline{wh}_l profile after the H profile is determined.

The latent heating effect results in the difference between \overline{wh}_l and \overline{ws}_v , as in the ENT/RAD/SFC/EVP (wet cloud) case shown in Figs. 1 and 10. (These two fluxes are identical in the "dust cloud" simulations.) The buoyancy flux \overline{ws}_v is of great importance since it is the major source for the turbulent kinetic energy. Comparing Figs. 1 and 10 indicates that latent heating contributes very little to the turbulent kinetic energy generation in this particular simulated case, which is stable with respect to cloud-top entrainment instability.

b. Partitioning the moisture flux

The moisture flux and its partitioning for all three stratus cases are given in Fig. 12. The total flux should be linear in height for a homogeneous, quasi-steady state. We assume its partitioned fluxes are also linear in height. Since radiation and latent heating do not change the total moisture field, the partitioning of the moisture flux is straightforward. The ENT curve is the component response to entrainment, while the SFC curve is that to the surface moisture flux. The sum (dotted lines) of these two curves agrees well with the \overline{wq}_T profile computed from the LES data (solid curves).

6. Summary and conclusions

We have analyzed four large-eddy simulations of idealized nocturnal, stratus-topped PBLs and the clear convective PBL. The simulations are designed so we can approximately isolate the physical processes of 1) cloud-top radiative cooling, 2) entrainment, 3) surface heating, and 4) latent heating and study their contributions to turbulent fluxes.

First, we showed that the turbulent fluxes of heat and moisture within the mixed stratus-topped bound-

ary layers are well expressed by the thermodynamic differences between updrafts and downdrafts of turbulent circulations. This is the basis for convective mass flux modeling, which has recently been applied to the buoyancy-driven PBL. We showed that the convective mass flux $M_c = 0.6\sigma_w$ is a good approximation, not only for clear boundary layers as suggested by Businger and Oncley (1990), but also for the heat and moisture transports throughout the stratus-topped mixed layer.

Therefore, we examined the contribution of each physical process to these differences between updrafts and downdrafts by conditional sampling of the large-eddy simulated fields. This gives us qualitative pictures of how each process contributes to the turbulent transports. Based on that, we quantitatively examined the linear process partitioning of the thermodynamic energy and moisture fluxes. First, we assumed that each process contributes linearly in height to H and \overline{wq}_T fluxes. We then showed that each component flux contributes to the net flux consistently (at all heights) with those summarized in section 4c. The cloud-top radiative cooling process gives a positive contribution to H , entrainment a negative one, and only when the former dominates the latter can the H flux remain positive in the absence of surface heating. In the mid-PBL of the ENT/RAD/SFC (dust cloud) case, the surface heating contributes efficiently to more than one-half of the H . The surface effect contributes about twice as much to the net moisture flux in the mid-PBL of the ENT/RAD/SFC case as compared with the ENT/RAD case. These consistencies provide a justification for the linear process-partitioning technique.

We also showed that by including only the *within-turbulent-layer* radiation effect does the sum of all component fluxes give an H -flux profile that agrees well with that computed directly from the LES data.

Therefore, the H profile can be determined from three quantities: the surface flux, $(\overline{wh}_l)_0$, the entrainment flux, $(\overline{wh}_l)_{z_i}$, and the bulk flux jump of longwave radiation across the whole *turbulent* layer, ΔF . After we determine H , we can then determine the vertical profile of \overline{wh}_l by subtracting F_{rad} from H , with F_{rad} as a prescribed forcing. This way, we include the effect of the vertically distributed longwave cooling on the turbulent transports, as pointed out by Randall (1980b), Lilly and Schubert (1980), and Hanson (1987b).

Similarly, we can determine the vertical profile of the total moisture flux \overline{wq}_T from $(\overline{wq}_T)_{z_i}$ and $(\overline{wq}_T)_0$. Together, \overline{wh}_l and \overline{wq}_T determine the buoyancy flux profile.

The main purpose of this paper is to show methods to identify the contributions of various processes to the updrafts and downdrafts and to the flux profiles given the entrainment rate, longwave radiation flux, and the surface flux. Whether the process partitioning technique can be used to determine the entrainment rate,

as proposed by Stage and Businger (1981), is beyond the scope of this paper.

Our discussions here are for a highly mixed buoyancy-driven PBL, where the dominant turbulent circulations fill the whole PBL. When the stratus cloud layer is decoupled from its subcloud layer (because of internal solar heating or drizzling), the turbulent circulations no longer fill the whole PBL and linear partitioning no longer applies.

Also, our discussions apply only to stratus-topped PBL that is stable with respect to the cloud-top entrainment instability. When the cloud-top evaporative cooling effect dominates, there is likely a strong en-

trainment–evaporation interaction. Stronger entrainment leads to larger cloud-top evaporative cooling with *more* cooling in the downdraft branch. This can lead to stronger turbulent circulations and consequently to an enhanced entrainment. Whether this positive feedback interaction will lead to a breakup of the stratus deck is still in debate (e.g., Hanson 1984; Kuo and Schubert 1988; Siems et al. 1990; Albrecht 1991). In the near future, we will analyze the large-eddy simulation of a stratus-topped PBL that is unstable with respect to this instability and examine this feedback mechanism.

Acknowledgments. We thank Joost Businger, Don

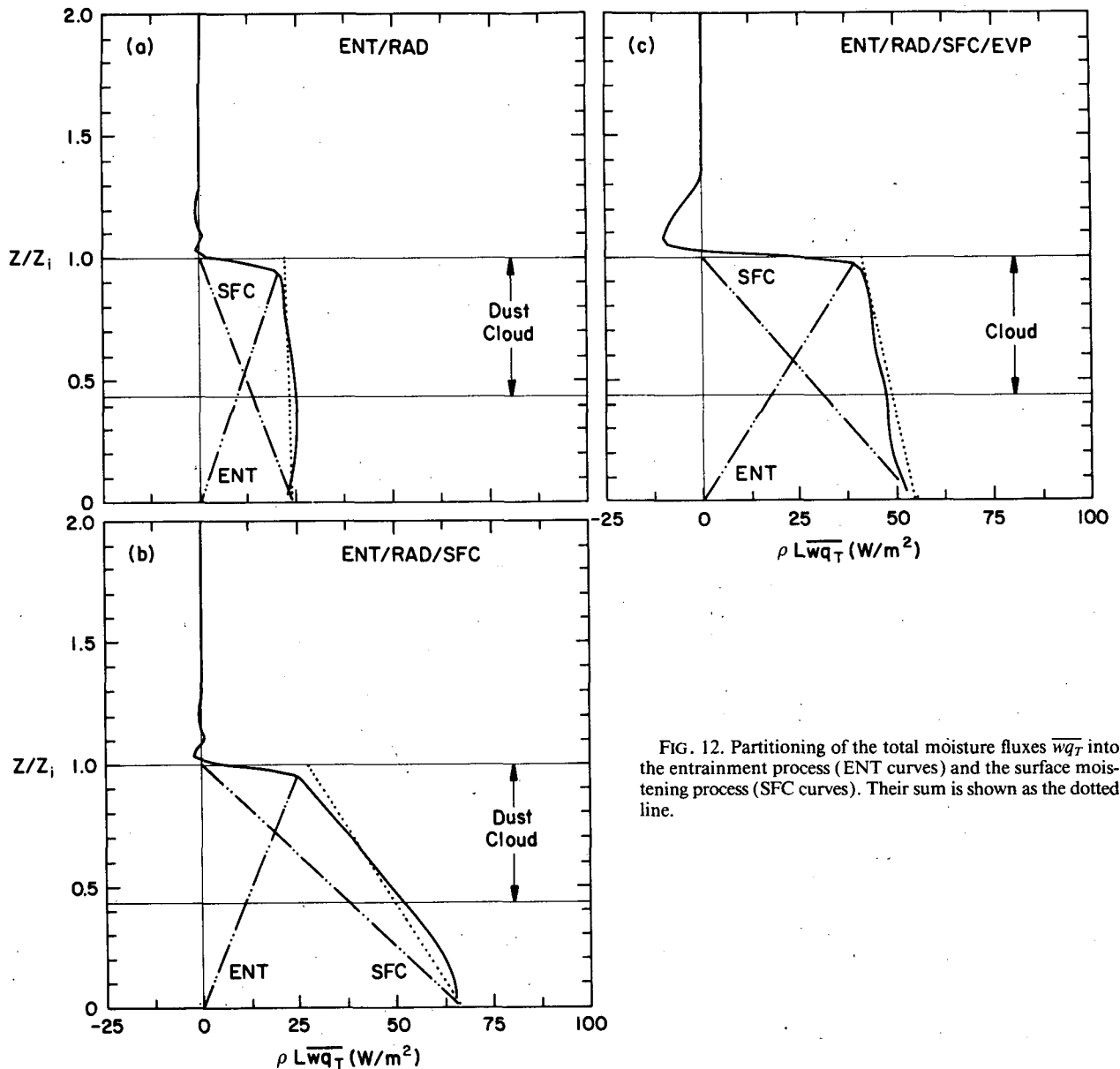


FIG. 12. Partitioning of the total moisture fluxes $\overline{wq_T}$ into the entrainment process (ENT curves) and the surface moistening process (SFC curves). Their sum is shown as the dotted line.

Lenschow, Ilga Paluch, Steve Siems, Steve Stage, Roland Stull, and George Young for helpful comments. C.-H. Moeng and S. Shen were partially supported by the Office of Naval Research under Interagency Agreement (IA) No. 89-12. D. Randall was partially supported by NASA's Climate Program under Grant NAG-1-893, and by the Office of Naval Research under Contract N00014-89-J-1364.

REFERENCES

- Albrecht, B. A., 1991: Fractional cloudiness and cloud-top entrainment instability. *J. Atmos. Sci.*, **48**, 1519–1525.
- , R. S. Penc, and W. H. Schubert, 1985: An observational study of cloud-topped mixed layers. *J. Atmos. Sci.*, **42**, 800–822.
- Arakawa, A., 1969: Parameterization of cumulus convection. *Proc. WMO/IUGG Symp. Numerical Weather Prediction*, Tokyo, Japan Meteor. Agency, **8**, 1–6.
- Betts, A. K., 1976: Modeling subcloud layer structure and interaction with a shallow cumulus layer. *J. Atmos. Sci.*, **33**, 2363–2382.
- Businger, J. A., and S. P. Oncley, 1990: Flux measurement with conditional sampling. *J. Atmos. Oceanic Technol.*, **7**, 349–352.
- Chatfield, R. B., and R. A. Brost, 1987: A two-stream model of the vertical transport of trace species in the convective boundary layer. *J. Geophys. Res.*, **92**, 13 263–13 276.
- Deardorff, J. W., 1974a: Three-dimensional numerical study of the height and mean structure of a heated boundary layer. *Bound.-Layer Meteor.*, **7**, 81–106.
- , 1974b: Three-dimensional numerical study of turbulence in an entraining mixed layer. *Bound.-Layer Meteor.*, **7**, 199–226.
- , 1980a: Stratocumulus-capped mixed layers derived from a three-dimensional model. *Bound.-Layer Meteor.*, **18**, 495–527.
- , 1980b: Cloud-top entrainment instability. *J. Atmos. Sci.*, **37**, 131–147.
- Greenhut, G. K., and S. J. S. Khalsa, 1987: Convective elements in the marine atmospheric boundary layer. Part I: Conditional sampling statistics. *J. Climate Appl. Meteor.*, **26**, 813–822.
- Hanson, H. P., 1984: Stratocumulus instability reconsidered: A search for a physical mechanism. *Tellus*, **36A**, 355–368.
- , 1987a: Reinterpretation of cloud-topped mixed-layer entrainment closure. *Tellus*, **39A**, 215–225.
- , 1987b: Radiative-turbulent transfer interactions in layer clouds. *J. Atmos. Sci.*, **44**, 1287–1295.
- Kahn, P. K., and J. A. Businger, 1979: The effect of radiative flux divergence on the entrainment of a saturated convective boundary layer. *Quart. J. Roy. Meteor. Soc.*, **105**, 303–306.
- Kuo, H., and W. H. Schubert, 1988: Stability of cloud-topped boundary layers. *Quart. J. Roy. Meteor. Soc.*, **114**, 887–917.
- Lilly, D. K., 1968: Models of cloud-topped mixed layers under a strong inversion. *Quart. J. Roy. Meteor. Soc.*, **94**, 292–309.
- , and W. H. Schubert, 1980: The effects of radiative cooling in a cloud-topped mixed layer. *J. Atmos. Sci.*, **37**, 482–487.
- MacVean, M. K., and P. J. Mason, 1990: Cloud-top entrainment instability through small-scale mixing and its parameterization in numerical models. *J. Atmos. Sci.*, **47**, 1012–1030.
- Manins, P. C., and J. S. Turner, 1978: The relationship between the flux ratio and energy ratio in convectively mixed layers. *Quart. J. Roy. Meteor. Soc.*, **104**, 39–44.
- Moeng, C.-H., 1984: A large-eddy-simulation model for the study of planetary boundary-layer turbulence. *J. Atmos. Sci.*, **41**, 2052–2062.
- , 1986: Large-eddy simulation of a stratus-topped boundary layer. Part I: Structure and budgets. *J. Atmos. Sci.*, **43**, 2886–2900.
- , 1987: Large-eddy simulation of a stratus-topped boundary layer. Part II: Implications for mixed-layer modeling. *J. Atmos. Sci.*, **44**, 1605–1614.
- , and J. C. Wyngaard, 1984: Statistics of conservative scalars in the convective boundary layer. *J. Atmos. Sci.*, **41**, 3161–3169.
- , and —, 1986: An analysis of closures for pressure-scalar covariances in the convective boundary layer. *J. Atmos. Sci.*, **43**, 2499–2513.
- , and —, 1988: Spectral analysis of large-eddy simulations of the convective boundary layer. *J. Atmos. Sci.*, **45**, 3575–3587.
- , and —, 1989: Evaluation of turbulent transport and dissipation closures in second-order modeling. *J. Atmos. Sci.*, **46**, 2311–2330.
- , and U. Schumann, 1991: Composite structure of plumes in stratus-topped boundary layers. *J. Atmos. Sci.*, **48**, 2280–2291.
- Nicholls, S., 1989: The structure of radiatively driven convection in stratocumulus. *Quart. J. Roy. Meteor. Soc.*, **115**, 487–511.
- Nieuwstadt, F. T. M., and J. A. Businger, 1984: Radiative cooling near the top of a cloudy mixed layer. *Quart. J. Roy. Meteor. Soc.*, **110**, 1073–1078.
- Randall, D. A., 1980a: Conditional instability of the first kind upside-down. *J. Atmos. Sci.*, **37**, 125–130.
- , 1980b: Entrainment into a stratocumulus layer with distribution radiative cooling. *J. Atmos. Sci.*, **37**, 148–159.
- , 1984: Buoyant production and consumption of turbulence kinetic energy in cloud-topped mixed layers. *J. Atmos. Sci.*, **41**, 402–413.
- , 1987: Turbulent fluxes of liquid water and buoyancy in partly cloudy layers. *J. Atmos. Sci.*, **44**, 850–858.
- , Q. Shao, and C.-H. Moeng, 1992: A second-order bulk boundary-layer model. *J. Atmos. Sci.*, **49**, 1903–1923.
- Schumann, U., and C.-H. Moeng, 1991a: Plume fluxes in clear and cloudy convective boundary layers. *J. Atmos. Sci.*, **48**, 1746–1757.
- , and —, 1991b: Plume budgets in clear and cloudy convective boundary layers. *J. Atmos. Sci.*, **48**, 1758–1770.
- Siems, S. T., C. S. Bretherton, M. B. Baker, S. S. Shy, and R. E. Breidenthal, 1990: Buoyancy reversal and cloud-top entrainment instability. *Quart. J. Roy. Meteor. Soc.*, **116**, 705–739.
- Slingo, A., R. Brown, and C. L. Wrench, 1982: A field study of nocturnal stratocumulus III. High resolution radiative and microphysical observations. *Quart. J. Roy. Meteor. Soc.*, **108**, 145–165.
- Stage, S. A., and J. A. Businger, 1981: A model for entrainment into a cloud-topped marine boundary layer. Part I: Model description and application to a cold-air outbreak episode. *J. Atmos. Sci.*, **38**, 2213–2229.
- Stull, R. B., 1988: *An Introduction to Boundary Layer Meteorology*. Kluwer Academic, 571 pp.
- Wang, S., and B. A. Albrecht, 1990: A mean-gradient model of the dry convective boundary layer. *J. Atmos. Sci.*, **46**, 126–138.
- Wilczak, J. M., and J. A. Businger, 1983: Thermally indirect motions in the convective atmospheric boundary layer. *J. Atmos. Sci.*, **40**, 343–358.
- Wyngaard, J. C., Ed., 1984: *Large-Eddy Simulation: Guideline for its Application to Planetary Boundary Layer Research*. Available from DTIC, AD-A146381, 122 pp.
- , and C.-H. Moeng, 1992: Parameterizing turbulent diffusion through the joint probability density. *Bound.-Layer Meteor.*, **60**, 1–13.
- Young, G. S., 1988: Turbulence structure of the convective boundary layer. Part II: Phoenix 78 aircraft observations of thermals and their environment. *J. Atmos. Sci.*, **45**, 727–735.